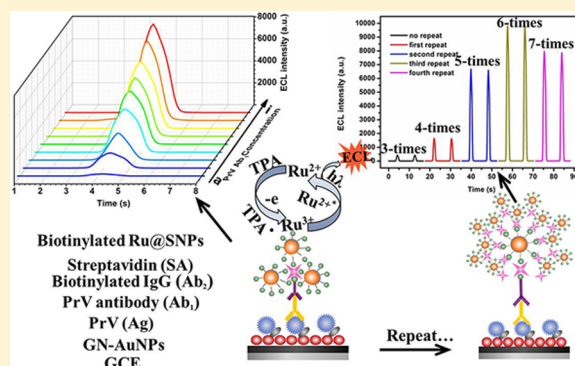# Stretch−Stowage−Growth Strategy to Fabricate Tunable Triply-Amplified Electrochemiluminescence Immunosensor for Ultrasensitive Detection of Pseudorabies Virus Antibody

Kang Shao, Jing Wang, Xiaochun Jiang, Feng Shao, Tingting Li, Shiyi Ye, Lu Chen, and Heyou Han*

State Key Laboratory of Agricultural Microbiology, College of Science, Huazhong Agricultural University, Wuhan 430070, P.R. China

S *Supporting Information*

ABSTRACT: Triply amplified electrochemical biosensors have attracted particular attention in the detection of low-abundance biomarkers. The universal construction routes for nonenzymatic triply amplified and even multiply amplified biosensors are extremely desirable but remain challenging. Here, we proposed a "stretch−stowage−growth" strategy to tunably fabricate a nonenzymatic triply amplified or multiply amplified electrochemiluminescence (ECL) immunosensor for ultrasensitive determining pseudorabies virus (PrV) antibody. Based on the matrix role of gold nanoparticle-graphene nanosheet (Au−GN) hybrids, carrier role of silicon nanoparticles (SNPs) and bridge role of "biotin−streptavidin−biotin" (B−SA−B) structure, the establishment processes were defined as "stretch", "stowage", and "growth", respectively. Relying on the interaction of antigen−antibody and of B-SA, the "Au−GN/PrV (Ag)/PrV antibody (Ab$_1$)/biotinylated IgG (B-Ab$_2$)/SA/biotinylated Ru(bpy)$_3^{2+}$-encapsulated SNPs (B−Ru@SNPs)" triply amplified biosensor could be fabricated and exhibited better analytical performance not only toward monoclonal PrV antibody with a linear detection range from 50 ng mL^{-1} to 1 pg mL^{-1} and a detection limit of 0.40 pg mL^{-1}, but also toward actual serum samples when compared with enzyme-linked immunosorbent assay and fluorometry. Furthermore, multiply amplified biosensors could be conveniently fabricated by controllably repeating the combination of B−Ru@SNPs and SA to form the B−SA−B structure. After it was repeated three times, the multiply amplified biosensor stretched to the maximum of signal amplification and achieved a luminescence quantum efficiency about 23.1-fold higher than the triply amplified biosensor. The tunable biosensor exhibits good stability, acceptable reproducibility and accuracy, suggesting its potential applications in clinical diagnostics.

Pseudorabies (PR), also known as Aujeszky's disease, is a seriously acute, widely infectious, frequently fatal disease that infects nearly all mammals except higher primates and humans.[1] It is characterized by nervous disorders, respiratory distress, severe weight loss, and high morbidity and mortality, leading to severe economic losses in animal husbandry worldwide, especially in the United States, Europe, and Asia.[2] Therefore, it is imperative to develop some simple, rapid, cost-effective, sensitive and reliable techniques to determine pseudorabies virus (PrV). In the past decade, a variety of strategies have been proposed for PrV analysis, mainly including virus neutralization test,[3] latex agglutination test (LAT), enzyme-linked immunosorbent assay (ELISA),[4] fluorescence analysis,[5] and polymerase chain reaction (PCR).[6] Although most of the aforementioned methods are reliable and effective, they usually suffer from serious drawbacks, such as insensitive, time-consuming and expensive. To overcome these drawbacks, a better alternative electrogenerated chemiluminescence (ECL) technology that combines electrochemical and luminescent methods has emerged and proved to be a powerful analytical technique for clinical diagnostics,[7] immunoassay[8] and

DNA analysis,[9] environmental assays,[10] as well as food and water testing.[11] However, this technique is unable to meet the requirements of early diagnosis of low-abundance biomarkers because of its sole dependence on inefficient self-luminous signal labels. Thus, signal amplification strategies have been developed for ECL trace analysis, such as immobilizing technique (Langmuir−Blodgett,[12] self-assembly,[13] sol−gel, and ion exchange polymer[14]), catalytic technique, bridging technique (typical biotin−avidin and DNA), and carrier technique.[15]
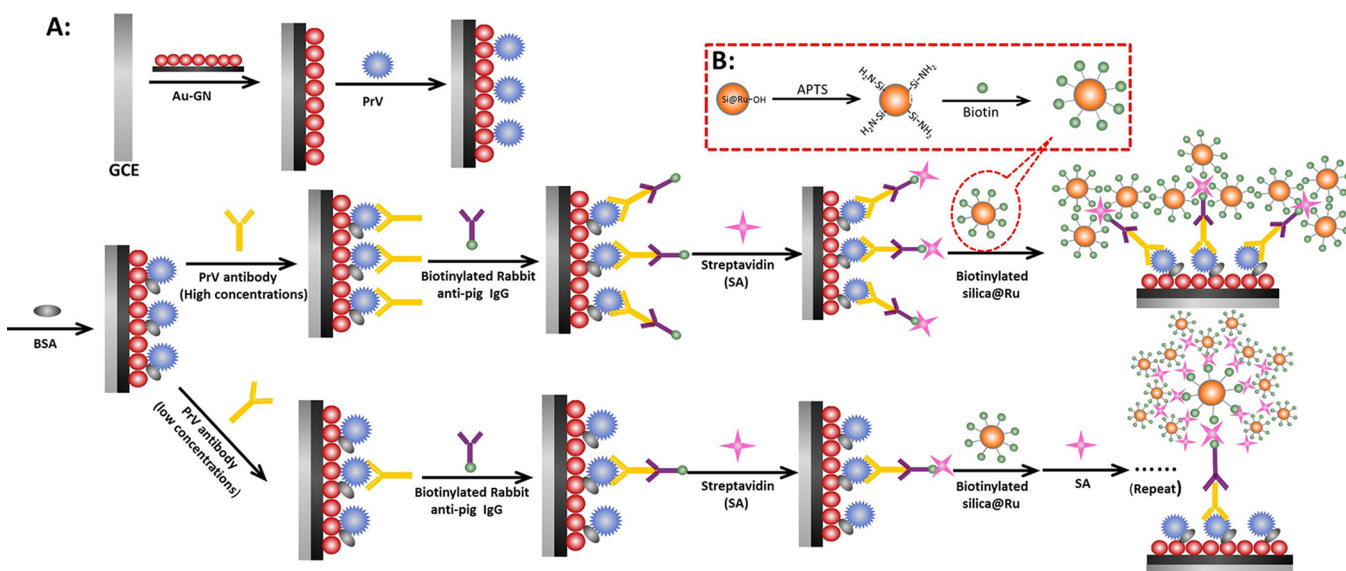
Signal amplification for ECL mainly involves three levels: the matrix, the luminescence quantum efficiency of signal labels, and the number of signal labels. Carbon materials (such as carbon nanotubes,[16] graphene,[17] carbon sphere[18] and carbon nanofiber[19]) and noble metal nanostructures are usually used as effective matrix for the indirect signal amplification.[8c] Moreover, based on the chemocatalysis of coreacted materials[20] and

Scheme 1. (A) Schematic Illustration of ECL Biosensor for Detection of PrV Antibody and (B) Fabrication Procedures of B—Ru@SNPs

enzyme catalysis,[8b] signal amplification could be achieved by accelerating the process of electrochemical redox reaction. Finally, signal intensity could also be enhanced by using some materials as good carriers or bridges to improve the loading number of signal labels, such as carbon carrier materials, metal and nonmetallic nanometerials (gold nanometerials,[21] silica microspheres,[22] iron-oxide nanoparticles,[23] etc.), high polymer (Nafion,[24] chitosan,[25] polystyrene microspheres,[26] etc.), and biomaterial (apoferritin,[27] liposome,[28] streptavidin,[29] etc.). The main amplified mechanisms of these aforementioned materials could be summarized into three categories: (i) the conductive matrixes with unique spatial structures can enhance the relative surface active region for further target assembling and accelerate the electron transfer among the electrode, signal labels and electrolyte; (ii) the active radicals or coreacted intermediates generated by the enzyme catalysis or chemocatalysis can participate in the electrochemical redox reaction of the signal labels and then drastically reduce the activation energy or improve effective collision (e.g., for electrochemistry: reducing the redox potential; for ECL, improving the luminescence quantum efficiency); (iii) various carriers with a larger specific surface or volume could fix more signal labels by means of physical absorption, electrostatic interaction or chemical reaction. On the basis of these mechanisms, researchers have designed a growing number of high-efficiency double signal amplification strategies for improving detection sensitivity by appropriate combination of different amplified materials, such as $Ru(bpy)_3^{2+}$-encapsulated silicon nanoparticles (Ru@SNPs)-gold nanoparticles (Au NPs),[30] multiwalled carbon nanotube (MWCNTs)-Ru@SNPs,[15a] and Ru@SNPs-DNA.[31]

However, the limited enlargement effect and the urgent demand of detection sensitivity for the early clinical diagnosis impelled researchers to develop further triple signal amplification. Recently, Han et al. have successfully achieved the triple signal amplification for trace detection of apurinic/apyrimidinic endonuclease (APE-1) by biocatalysis of alkaline phosphatase, chemicatalysis of nickel hexacyanoferrates nanoparticle-decorated Au nanochains (Ni-AuNCs) and interaction of biotin—streptavidin.[32] Hou et al. used DNAzyme-functionalized gold—

palladium hybrid nanotags as the triple amplified signal label for ultrasensitive detection of prostate-specific antigen (PSA) based on the carrier amplification, chemocatalysis and enzyme catalysis.[33] Without any involvement of enzymes, Ju's group designed a new triple signal amplification strategy based on graphene film, poly(styrene-*co*-acrylic acid) microbead (PSA) carried Au NPs and silver deposition for ultrasensitive immunosensing.[26] Just recently, another triply amplified biosensor has been proposed by replacing PSA with polybead mesoporous carbon foam.[34] Although some triply amplified biosensors are designed step by step, reports concerning multiply amplified biosensors and the universal or regular construction route of triply amplified biosensor are relatively scarce. Additionally, the limited magnification or untunability of most biosensors hinders their further application to variable and low-abundance biomarkers in the actual serum samples.

Herein, we proposed a versatile stretch—stowage—growth strategy to fabricate the nonenzymatic, triply amplified and tunable ECL immunosensor for ultrasensitive detection of PrV antibody in the actual swine serum samples (Scheme 1). Because PrV is often distributed in the organism's tissues and the duration of PrV in the blood is relatively short, leading to difficulties in sampling and detection. Thus, detecting PrV antibodies can be used as the important indicator of clinical diagnosis to reflect the situation of PrV. On the basis of gold nanoparticle-graphene nanosheet (Au—GN) hybrids, silica nanoparticles and biotin—streptavidin (B-SA), the triple or multiple signal amplification was achieved without any other amplifier media. Au—GN hybrids were utilized for the first amplification in the "stretch" step as graphene nanosheet (GN) has one-atom-thick and two-dimensional honeycomb layers of carbon networks and Au NPs could bind to most biological samples.[35] In the second step named as stowage, with easy modification and functionalization on the surface, silica nanoparticles could be used as a good carrier for $Ru(bpy)_3^{2+}$ to promote ECL detection.[36] Since streptavidin (SA) is a tetrameric protein containing four binding sites for biotin with extraordinarily high affinity ($K_d = 10^{-15}$), the biotinylated Ru@SNPs (B—Ru@SNPs) were fixed with biotinylated IgG (B-Ab$_2$) via bridge molecules SA. In the third step of growth, the B—

SA–B (biotin–streptavidin–biotin) structure was formed just like the growth of a branch. Then, the preliminary structure of biosensor was completed by interactions of antigen–antibody and biotin–streptavidin. However, for the active biotins that were modified on the surface of silica nanosphere, a part of biotins are bound to the SA and the remaining biotins can be used for further connection. Therefore, when the target concentration was low, the further multiple-amplification would proceed by repeating the B–SA–B construction process. By controlling the number of repetition, the signal response of ECL detection could remain at a high level whether with a high or low target concentration. Thus, the novel ECL biosensor was successfully applied to detection of PrV antibody in swine serum samples and presented an excellent performance.

■ EXPERIMENTAL SECTION

Reagents. The rabbit antipig IgG/biotin (B-Ab$_2$, 1 mg mL^{-1}) was purchased from Sangon biotech Co. Ltd. (Shanghai, China). The biotin-goat antimouse IgG (B-Ab$_2$, 1 mg mL^{-1}) was purchased from Proteintech Biotech Co. Ltd. (Wuhan, China). The pseudorabies MoAb ascites fluid IgG$_{2b}$ isotype (Ab$_1$, 1 mg mL^{-1}) was purchased from Veterinary Medical Research & Development (U.S.A.). The PrV (Ag, 10^6 PFU mL^{-1}) and the 17 clinical serum samples used were obtained from the State Key Laboratory of Agricultural Microbiology of Huazhong Agricultural University (Wuhan, China). The PrV positive serum and negative serum samples (ELISA kit) were obtained from Wuhan Keqian Animal Biological Products Co. Ltd. (China).

Tris(2,2′-bipyridyl) dichlororuthenium(II) hexahydrate (Ru-(BPY)$_3$, 99.95% trace metals basis), tetraethoxysilane (TEOS), Biotinamidohexanoic acid N-hydroxysuccinimide ester (B–NHS) (98%, powder), TritonX-100, (3-aminopropyl)-triethoxysilane (APTS), bovine serum albumin (BSA), poly-(diallyldimethylammonium chloride) (PDDA), were obtained from Sigma-Aldrich Chemicals Co. Chloroauric acid (HAuCl$_4$), trisodium citrate, graphite powder, H$_2$O$_2$ (30%), cyclohexane (GR), 1-hexanol, NH$_3$·H$_2$O (GR), N,N-dimethylformamide (DMF) and Tween-20 were obtained from Sinopharm Chemical Regent Co. Ltd. (Shanghai, China). Tri-n-propyl-amine (TPA) and streptavidin (SA, 17 units/mg protein) were obtained from Aladdin Chemical Co. Ltd. (Shanghai, China). All other common solvents and salts were of analytical grade and used as received. Phosphate buffered saline (PBS) was prepared by mixing PB solution with 0.9% NaCl. Ultrapure water (Mill-Q, Millipore, 18.2 MΩ cm resistivity) was used throughout the experiments.

Apparatus. The ECL emissions were recorded using a Model MPI-EII ECL Analyzer (Xi'an Remex Electronic Science & Technology Co. Ltd., China). All ECL experiments were performed in a 10 mL glass cell with a conventional three-electrode system composed of a platinum wire as the auxiliary electrode, Ag/AgCl (saturated KCl) electrode as the reference electrode and bare or modified glass carbon electrodes (GCE, 3 mm diameter) as the working electrodes.

Cyclic voltammetry (CV) and electrochemical impedance spectroscopy (EIS) analyses were performed with a CHI 660D electrochemical workstation (CH Instrument Co. Shanghai) in the solution of 0.5 M KCl containing 5 mM $K_3[Fe(CN)_6]$/$K_4[Fe(CN)_6]$, using the same three-electrode system in the ECL detection.

Ultraviolet–visible (UV–vis) absorption spectra were recorded on a Nicolet Evolution 300 Ultraviolet–visible

spectrometer coupled with a 1.00 cm quartz cell (Thermo Nicolet, US). Photoluminescence (PL) spectra were measured on an Edinburgh FLS920 spectrometer with an integrating-sphere attachment under excitation of 450 nm light. Fourier-transform infrared (FT-IR) spectra were collected on a Nicolet Avatar-330 spectrometer with 4 cm^{-1} resolution using the KBr pellet technique. Raman spectra were recorded with an inVia Raman spectrometer (Renishaw, UK) equipped with a He–Ne laser excitation source operating at 633 nm. Fluorescence microscopy images were obtained with an inverted fluorescence microscope (Eclipse Ti, Nikon). The ζ potential was measured with a Zeta-sizer Nano ZS90 DLS system (Malvern, England). Transmission electron microscopy (TEM) images were acquired using a FEI Tecnai G20 transmission electron microscope operating at an acceleration voltage of 200 kV.

The morphology of B–Ru@SNPs and the assembling process of the sandwiched immunosensor were characterized using field-emission scanning electron microscopy (FE-SEM, JSM-6700F, Japan).

Preparation of Au–GN Hybrids and Biotinylated Ru@SNPs. Au NPs, graphene nanosheets functionalized by PDDA (GN–PDDA), Au–GN hybrids, and Ru@SNPs were synthesized as previously reported.[25,37] The Ru@SNPs were redispersed with ethanol to a final volume of 6 mL. The detailed preparation processes are described in Supporting Information.

Scheme 1B shows the proposed formation process for biotinylated Ru@SNPs (B–Ru@SNPs). First, 1 mL of Ru@SNPs ethanol suspension reacted with 5 μL of APTS at room temperature for 12 h with continuous stirring.[38] The nano-particles were then separated by centrifugation and rinsed thoroughly with ethanol and 0.01 M PB (pH = 7.4) solution to remove excess APTS. The amino-functionalized Ru@SNPs (NH$_2$–Ru@SNPs) were obtained and dispersed into 1 mL of 0.01 M PB solution. Subsequently, 1 mg of biotinamidohex-anoic acid n-hydroxysuccinimide ester (B–NHS) was dissolved in 1 mL of DMF and then mixed with the NH$_2$–Ru@SNPs suspension. The reaction was maintained at 37 °C for 12 h under stirring. After the mixture was centrifuged and washed with DMF and water, the B–Ru@SNPs were obtained and dispersed with 0.01 M of pH 7.4 PB solution to a final volume of 5 mL for later use.[22]

Fabrication of the Ag–Ab$_1$–Ab$_2$ Sandwich Biosensor. Scheme 1A represents the preparation of the biosensor. The polished and subsequently washed glassy carbon electrode (GCE, diameter of 3 mm) was dried with high-purity nitrogen gas for the next modification process. Six microliters of Au–GN hybrid solution was pipetted onto the center of the pretreated GCE and allowed the casting solution to dry at room temperature for over 4 h. Then the Au–GN/GCE was washed 3 times with PBST (PBS with 0.05% Tween 20, pH 7.4) to remove the unabsorbed materials. After that, 10 mL of PrV suspension diluted 50-fold (0.01 M PBS, pH 7.4) was pipetted onto the Au–GN/GCE surface and then covered with a pipet tip for 12 h at 4 °C. Next, the modified electrode was rinsed with PBST to remove physically absorbed antigen and then incubated in 100 μL 1% BSA solution for 1 h at 37 °C to block possible remaining active sites and avoid the nonspecific adsorption. After washing thoroughly with PBST, the BSA/PrV/Au–GN/GCE was incubated in 60 μL of PrV antibody suspension for 50 min at 37 °C and then washed with PBST. Finally, the Ab$_1$/BSA/PrV/Au–GN/GCE was incubated in 100 μL of biotinylated rabbit antipig IgG or biotin-goat antimouse
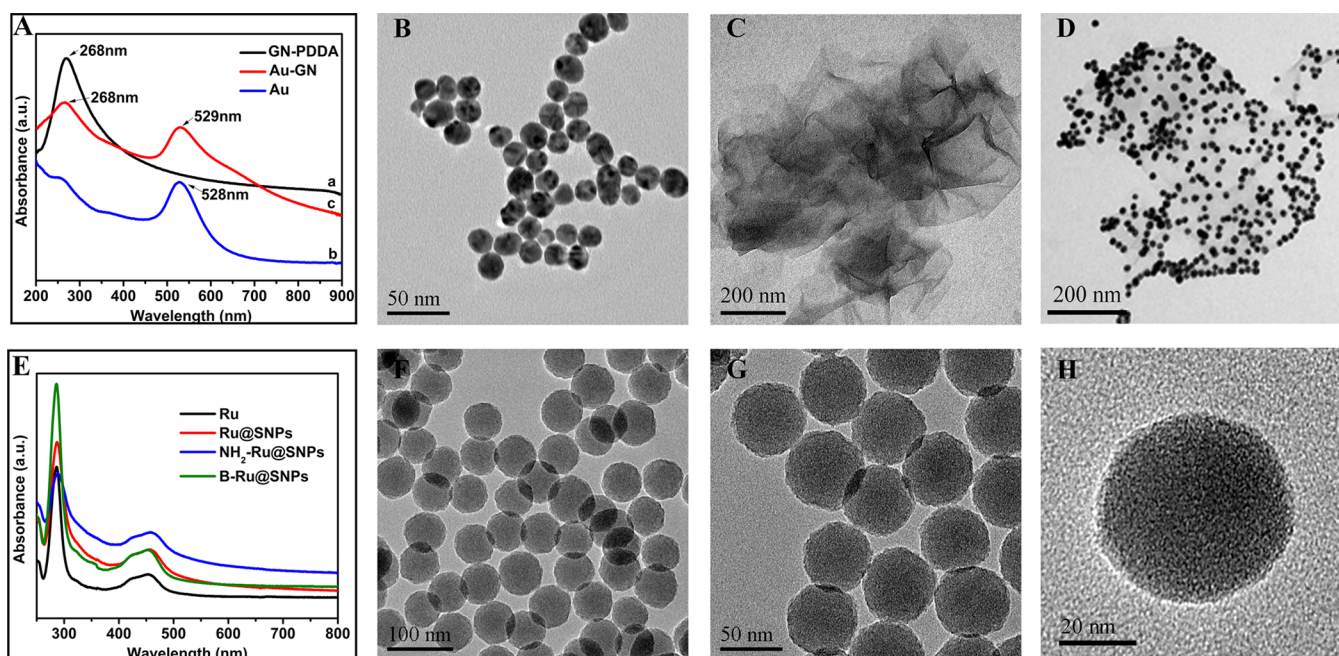
Figure 1. UV−vis absorption spectra (A) and TEM images of (B) Au NPs, (C) GN−PDDA, and (D) Au−GN hybrids. UV−vis absorption spectra of (E) Ru(BPY)$_3$, Ru@SNPs, NH$_2$−Ru@SNPs, and B−Ru@SNPs. TEM images of Ru@SNPs (F) 100, (G) 50, and (H) 20 nm.

IgG (B-Ab$_2$) for 60 min at 37 °C based on the type of PrV antibody, and then washed thoroughly with PBST to remove nonspecifically bounded conjugates for the subsequent ECL characterization assays.

ECL Characterization Assays. The B-Ab$_2$/Ab$_1$/BSA/PrV/Au−GN/GCE was incubated in 100 μL of 0.1 mg mL^{-1} SA for 60 min at 37 °C and then washed thoroughly with PBST. Next, the SA/B-Ab$_2$/Ab$_1$/BSA/PrV/Au−GN/GCE was incubated in 100 μL of B−Ru@SNPs for 60 min at 37 °C and then washed three times with PBST. Finally, the above two steps were repeated several times based on the need of signal amplification. Thus, the modified electrode was characterized via ECL measurement in a 0.1 M PB solution (pH 7.4) with 10 mM TPA using the aforementioned three-electrode system. The ECL measurements were performed from 0 to 1.3 V at a scan rate of 300 mV s^{-1}.

RESULTS AND DISCUSSION

Characterization of the Au−GN Hybrids and Ru@ SNPs. FT-IR spectroscopy was used to investigate the reduction and functionalization process of GN. As shown in Supporting Information Figure S1, the spectrum of graphene oxide (GO) showed the presence of C=O ($\nu_{C=O}$ at 1730 cm^{-1} in carbonyl groups), C=C ($\nu_{C=C}$ at 1633 cm^{-1}), and C−O (ν_{C-O} at 1150 cm^{-1}).[39] After the reduction process of GN, the dramatical decrease or disappearance of characteristic peaks of oxide groups indicated that such graphene oxides had been successfully reduced to the graphene. The absorption bands of GN−PDDA at 2932 (CH$_n$), 1648 (C=C), and 1464 cm^{-1} (C=C) corresponded to the characteristic bands of PDDA, showing the accomplishment of the functionalization of graphene with PDDA.[40] Raman spectroscopy was also used to characterize graphite powder, GO and GN−PDDA. It can be seen from Supporting Information Figure S2 that the D/G intensity ratio of GN−PDDA increased notably in comparison with that of GO, indicating an increase in the number of smaller graphitic domains upon reduction.[41] The photos of Au−GN

hybrids synthesized with different proportions of Au NPs and GN−PDDA are represented in Supporting Information Figure S3. The mixture of Au NPs and GN−PDDA at an Au/GN volume ratio of 50:1 had an excellent color and suspension, indicating an optimal mixing-ratio. The obtained Au−GN hybrid architecture was confirmed by the UV−vis absorption spectrum. As displayed in Figure 1A, the citrate-stabilized colloidal Au NPs (curve a) showed a strong characteristic absorption peak at 528 nm due to surface plasmon resonance. The GN−PDDA (curve b) exhibited a strong absorption peak at 270 nm due to $\pi \rightarrow \pi^*$ transitions of aromatic C=C bond, indicating the restoration of the π-conjugation network of the graphene nanosheets. After mixing the Au NPs and GN−PDDA at an optimal ratio, the characteristic peak of Au NPs was observed in Au−GN (curve c) at 529 nm, indicating the efficient adsorption of Au NPs onto the nanosheet surface. Moreover, the TEM images of the Au NPs, GN−PDDA and Au−GN hybrids also indicated the successful formation of hybrids (Figure 1B, Figure 1C and Figure 1D). Almost all anchored Au NPs (∼30 nm) were uniformly distributed across the thin flake-like GN−PDDA with some corrugation, suggesting a flexible structure of the nanosheets.

The typical W/O microemulsion method was used for preparing Ru@SNPs.[25] The water droplets containing Ru-(bpy)$_3$$^{2+}$ were stabilized and dispersed in bulk oil by surfactant molecules. With the highly regulated nucleation and growth kinetics of the silica on the surface of the water droplets, Ru(bpy)$_3$$^{2+}$ was successfully encapsulated in the silica network for the production of highly monodisperse Ru@SNPs. As displayed in Figure 1F−1H, the obtained Ru@SNPs presented a uniform and porous spherical structure with a diameter of 50 ± 3 nm. Supporting Information Figure S4 shows the photos and PL emission spectra of silica nanoparticles. When compared with milky silica nanoparticles with no peak, the obvious orange color and PL emission peak of Ru@SNPs suggested that Ru(bpy)$_3$$^{2+}$ was successfully entrapped inside of SiO$_2$ nanospheres and the entrapped Ru(bpy)$_3$$^{2+}$ also retained
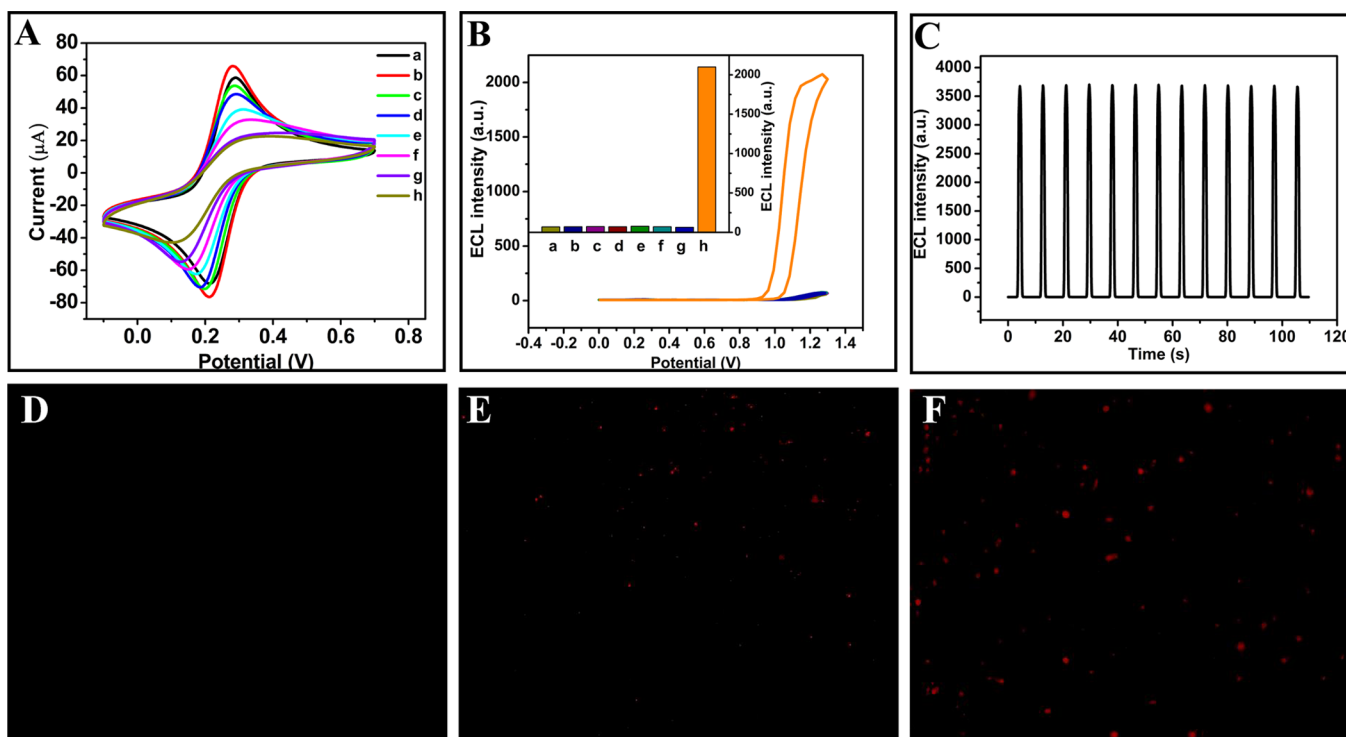
Figure 2. CV (A) and ECL-potential curves (B) of (a) bare GCE, (b) Au−GN/GCE, (c) Ag/Au−GN/GCE, (d) BSA/Ag/Au−GN/GCE, (e) Ab$_1$/BSA/Ag/Au−GN/GCE, (f) B-Ab$_2$/Ab$_1$/BSA/Ag/Au−GN/GCE, (g) SA/B-Ab$_2$/Ab$_1$/BSA/Ag/Au−GN/GCE, (h) B−Ru@SNPs/SA/B-Ab$_2$/Ab$_1$/BSA/Ag/Au−GN/GCE at the PrV Antibody concentration of 10 pg mL^{-1}. (C) ECL emission from B−Ru@SNPs/SA/B-Ab$_2$/Ab$_1$/BSA/Ag/Au−GN/GCE under continuous CVs for 14 cycles (100 pg mL^{-1}). Fluorescence microscope of (D) SA/B-Ab$_2$/Ab$_1$/BSA/Ag/Au−GN/GCE (E) B−Ru@SNPs/SA/B-Ab$_2$/Ab$_1$/BSA/Ag/Au−GN/GCE (F) B−Ru@SNPs/SA/B−Ru@SNPs/SA/B-Ab$_2$/Ab$_1$/BSA/Ag/Au−GN/GCE.

its good optical properties. The functionalization of amino-groups and the subsequent modification of biotin onto Ru@SNPs were first illustrated by the ζ potential measurement, with a mean zeta potential of −33.1 mV for the as-prepared Ru@SNPs. However, after reaction with APTS, the zeta potential dramatically changed from negative to positive (+14.6 mV) owing to the successful functionalization of amino-groups onto the surface of Ru@SNPs. After modification with B−NHS, the surface potential was significantly increased from +14.6 to +25.9 mV because of the introduction of more nitrogen atoms. Thus, the measurement of ζ potential preliminarily indicated that B−Ru@SNPs had been obtained successfully by reaction B−NHS with functional amino-groups on the surface of Ru@SNPs. FT-IR spectroscopy was used to further confirm the successful modification. Supporting Information Figure S5 reveals that the strong peak at 1100 cm^{-1} was ascribed to the Si−O−Si stretching vibration.[42] Compared with the absorption bands of amino-functionalized Ru@SNPs (NH$_2$−Ru@SNPs) at 1640 cm^{-1} (N−H) and other characteristic absorption bands of N−H at 960, 800, and 560 cm^{-1}, clear changes occurred after the amide formation by reaction of B−NHS and NH$_2$−Ru@SNPs. The disappearance of other characteristic absorption bands of N−H (amine) and the occurrence of the characteristic absorption bands at 1644 cm^{-1} (C=O) and 1520−1559 cm^{-1} (N−H, amide) indicated the successful preparation of B−Ru@SNPs. Photoluminescence (PL) spectra (Supporting Information Figure S6) and UV−vis absorption spectrum (Figure 1E) were used for investigating the performance of Ru@SNPs after functionalization and modification. As can be seen in Figure1E, Ru(bpy)$_3$$^{2+}$, Ru@SNPs, NH$_2$−Ru@SNPs, and B−Ru@SNPs all exhibited two charac-

teristic peaks at 285 and 450 nm, which were assigned to ligand-centered ($\pi \rightarrow \pi^*$) transitions and metal-to-ligand charge transfer adsorption, respectively.[43] The slightly reduced fluorescence intensity and identical UV−vis absorption peaks clearly manifested that the functionalization of Ru@SNPs was stable and reliable without any impact on the performance of Ru@SNPs.

Characterization of the ECL Immunosensor. Cyclic voltammetry (CV) and electrochemical impedance spectroscopy (EIS) were employed to verify the assembly process of the modified electrodes step by step. Figure 2A shows the CV curves to characterize the fabrication procedures of the modified GCE using $[Fe(CN)_6]^{4-}/[Fe(CN)_6]^{3-}$ as electroactive probes. The bare GCE exhibited a couple of reversible redox peaks in curve a. After the electrode was modified with Au−GN, the peak currents of the electrode increased obviously. Conversely, the potential difference (ΔE) clearly decreased between oxidation peak and reduction peak (curve b). The better performance of the modified electrode was attributed to the larger surface and the excellent electrical conductivity of Au−GN. When PrV was immobilized onto the Au−GN/GCE, an obvious decrease in the amperometric signal was found (curve c). With a further decrease in the peak currents in the CV, the gap between the anodic and cathodic peaks became wider in the subsequent stepwise construction process of Ab$_1$, BSA, Ab$_2$, SA and B−Ru@SNPs. This phenomenon resulted from the electron inert feature of Ab$_1$, BSA, Ab$_2$, SA, and B−Ru@SNPs, blocking the electron transfer and mass transfer of $[Fe(CN)_6]^{4-}/[Fe(CN)_6]^{3-}$ ions at the Au−GN/GCE surface. These changes obviously showed the successful fabrication of ECL biosensor for detection of PrV.
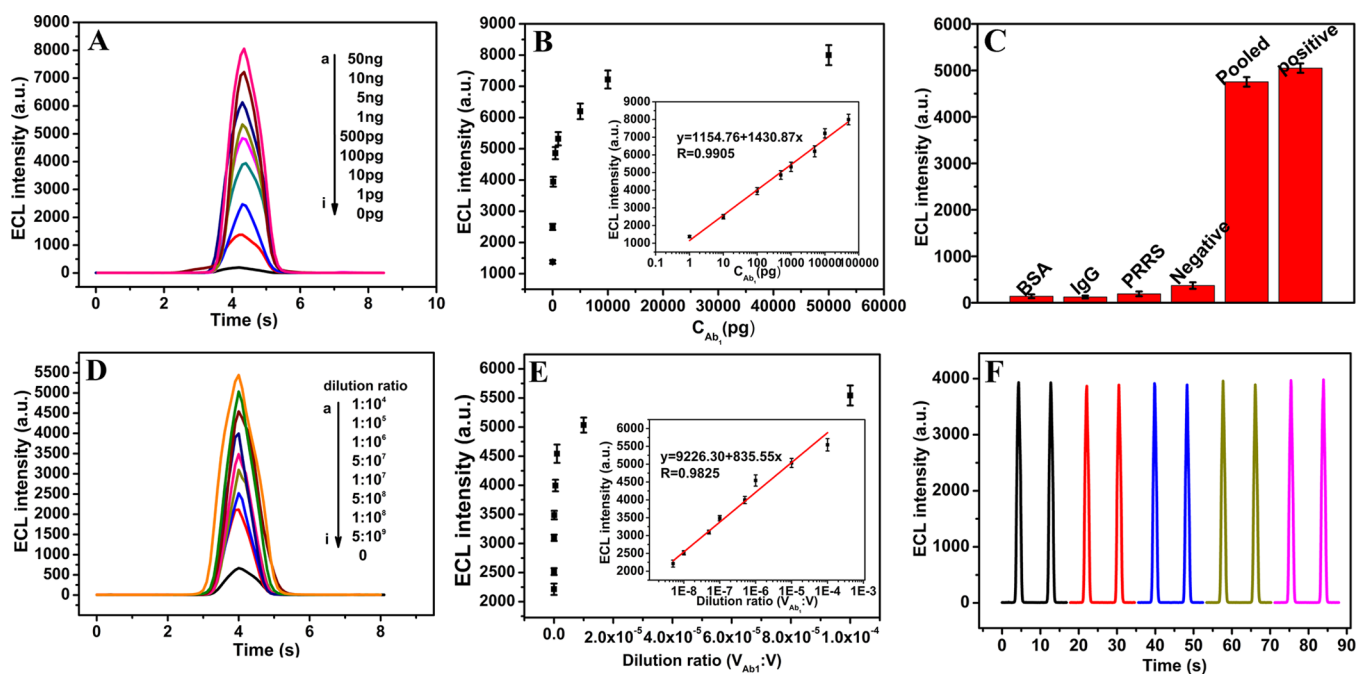
Figure 3. (A) ECL profiles of the biosensor at different concentrations of monoclonal PrV antibody (a) 50 ng, (b) 10 ng, (c) 5 ng, (d) 1 ng, (e) 500 pg, (f) 100 pg, (g) 10 pg, (h) 1 pg, and (i) 0 pg in 0.1 M pH 7.4 PB solution containing 0.01 M TPA scanning from 0 to 1.3 V at a scan rate of 300 mVs^{-1}. (B) Calibration curve for determination of monoclonal PrV antibody. (C) Specificity of BSA, IgG, PRRS, negative serum, pooled serum (positive serum/negative serum = 1:1), and positive serum. (D) ECL profiles of the biosensor at different concentrations of polyclone PrV antibody (a) 1:10^4, (b) 1:10^5, (c) 1:10^6, (d) 5:10^7, (e) 1:10^7, (f) 5:10^8, (g) 1:10^8, (h) 5:10^9, and (i) 0. (E) Calibration curve for determination of polyclone PrV antibodies. (F) Reproducibility of five B−Ru@SNPs/SA/B-Ab$_2$/Ab$_1$/BSA/Ag/Au−GN/GCE at an identical concentration of PrV antibody.

Additionally, EIS was also used for monitoring the changes in the surface features of the modified electrodes in the assembly process (Supporting Information Figure S7). The diameter of the semicircle in a higher frequency range of the niquist plots equals to the electron transfer resistance (R_{et}) at the electrode interface. The Au−GN/GCE exhibited a lower R_{et} than bare GCE due to the good electronic transfer capability (curve a, b). With the sequential assembly of PrV (curve c), Ab$_1$ (curve d), BSA (curve e), Ab$_2$ (curve f), SA (curve g) and B−Ru@SNPs (curve h), the R_{et} increased steadily. The result of EIS was consistent with the CV, confirming the successful preparation of the biosensor.

The sandwiched immunoassay was further confirmed by ECL measurements (Figure 2B). No ECL signals were observed on the successively assembled GCE until the SA/B-Ab$_2$/Ab$_1$/BSA/Ag/Au−GN/GCE was incubated in B−Ru@SNPs solution (curve a, b, c, d, e, and f). The occurrence of a strong ECL signal indicated that the electrochemiluminescent substrate was captured successfully on the electrode surface and exhibited excellent performance for ECL analysis (curve g). The corresponding CV curve is shown in Supporting Information Figure S8. The current peak associated with the direct oxidation of TPA occurred in the potential region more positive than 0.7 V. Then with the oxidation of Ru(bpy)$_3^{2+}$ beyond 1.0 V, a main ECL peak appeared at ~1.15 V.[44] Furthermore, the ECL intensities of the immunosensor incubated in PrV antibody solution (concentration 1 ng mL^{-1}) for 50 min remained comparatively stable during consecutive cyclic potential scanning, indicating an acceptable stability for ECL detection (Figure 2C).

The fluorescence microscopy images and scanning electron microscope (SEM) images also confirmed the successful assembly of the ECL immunosensor. The scattered fluores-

cence spheres with an orange color were observed apparently on the B−Ru@SNPs/SA/B-Ab$_2$/Ab$_1$/BSA/Ag/Au−GN/GCE at a monoclonal antibody (Ab$_1$) concentration of 1 ng mL^{-1} (Figure 2D and Figure 2E). More and larger orange fluorescence spheres were observed on the electrode by repeating the modification of SA and B−Ru@SNPs (Figure 2F). These results not only proved the successful assembly of the biosensor but also confirmed the feasibility of modification repetition. The main assembling procedures of the sandwiched immunosensor are demonstrated in Supporting Information Figure S9, showing that many spherical PrVs with a diameter of 150−200 nm and spherical B−Ru@SNPs with a diameter about 50 nm were connected on the biological samples (image A-I), also confirming the successful assembly of the biosensor.

Characterization of the ECL Detection of Monoclonal PrV Antibody. The ECL performance of this biosensor was closely related to the incubation time of Ab$_1$ and the pH of PB solution, and thus a series of optimization experiments were carried out concerning the two variables. As shown in Supporting Information Figures S10 and S11, the ECL signal of the biosensor increased obviously with the incubation time of Ab$_1$, but was found to be a steady value after 50 min. Additionally, the maximum ECL response of the biosensor occurred at a pH close to 7.4. Therefore, the optimal incubation time of Ab$_1$ was 50 min and the optimal pH of PB solution was 7.4.

Under the aforementioned optimized conditions, the ECL behavior of the biosensor for detection of PrV antibody was investigated in 0.1 M PB solution with 10 mM TPA. Figure 3A shows the ECL signal of biosensor corresponding to monoclonal PrV antibody at different concentrations. The ECL signal intensities gradually decreased with decreasing concentrations of monoclonal PrV antibodies, indicating a good

biocompatibility of the biosensor and an excellent capability in response to target changes. The standard calibration curve for detection of PrV antibody is illustrated in Figure 3B. The ECL peak intensities are proportional to the logarithmic value of the PrV antibody concentrations over a range from 50 ng mL^{-1} to 1 pg mL^{-1}. The linear regression equation is I_{ECL} (au) = 1430.87 × log C_{Ab1} + 1154.76 with the correlation coefficient R = 0.9905, where I_{ECL} is the ECL peak intensity and C_{Ab1} is the PrV monoclonal antibody concentration. The detection limit was roughly calculated to be 0.40 pg mL^{-1} with a signal-to-noise ratio of 3.

Detection of PrV Polyclonal Antibody in Swine Serum Sample. To evaluate the detection effect of the actual swine serum samples, a series of positive serum samples from ELISA kit were examined at a different dilution ratio. Figure 3D shows the ECL signal of the biosensor corresponding to polyclonal PrV antibody in positive swine serum samples at a different dilution ratio. The ECL signal intensities gradually decreased with decreasing concentration of polyclonal PrV antibodies. This result also confirmed that the biosensor had an excellent capability in response to changes of the actual serum samples. The standard calibration curve for detection of polyclonal PrV antibody in swine serums is illustrated in Figure 3E. The linear regression equation is I_{ECL} (au) = 835.55 × log C_{Ab1} + 9226.30 with the correlation coefficient R = 0.9825, where I_{ECL} is the ECL peak intensity and C_{Ab1} is the PrV polyclonal antibody concentration.

Specificity, Reproducibility, and Stability of the Biosensor. The specificity of the biosensor for the clinical samples was tested by contrasting positive serum (from piglet infected with PrV) with negative serum (from piglet not infected with PrV) samples, pooled serum (positive serum/ negative serum = 1:1), porcine reproductive and respiratory syndrome (PRRS), IgG and BSA at the same concentration. As shown in Figure 3C, two stronger ECL signals were obtained for the positive serum and pooled serum and only very weak signals emerged for negative serum, IgG and BSA. Addtionally, the two stronger ECL signals were fitted to the linear regression equation. The results demonstrated that the proposed ECL biosensor had a good feasibility and selectivity. The reproducibility of the biosensor was investigated with intra- and interassay precision. The intra-assay precision was investigated by assaying one PrV antibody level (dilution ratio 1:10^7) for five similar measurements (Figure 3F). The similar ECL intensity demonstrated that the biosensor possessed an acceptable reproducibility. Furthermore, the biosensor was found to retain 89% of the original ECL response after 10 days of storage in 0.01 M PB solution at 4 °C.

The recovery test was performed using the PrV negative and positive serum samples with the standard addition method. Each recovery of PrV antibody was determined by comparing the results obtained before and after adding the monoclonal PrV antibody to the diluted serum samples of the mouse. The results are presented in Table 1. The recoveries of serum samples at a different level of antibody ranged from 91.1% to 109.2% with an analytical precision of RSD ≤ 5.0%, thereby validating the reliability and practicality of this method.

Diagnostic Performance by Qualitative and Quantitative Analyses. To estimate the diagnostic performance of the proposed method, 17 clinical serum samples collected from infected pigs were analyzed by both the ECL immune method and ELISA without any reference test to classify the pigs as truly infected or noninfected. The results are shown in Figure 4

Table 1. Standard Addition Recovery Experiments of the Monoclonal PrV

sample	added (pg mL^{-1})	detected (pg mL^{-1})	recovery (pg mL^{-1})	RSD (%, n = 5)
1	0	8.31		
	10	17.54 ± 0.38	92.3	3.8
	20	30.16 ± 0.84	109.2	4.2
2	0	29.23		
	50	74.78 ± 2.45	91.1	4.9
	100	135.82 ± 3.67	106.6	3.7

and Supporting Information Table S1. Compared with ELISA, the proposed ECL method has a higher sensitivity and specificity for the detection of PrV antibody.
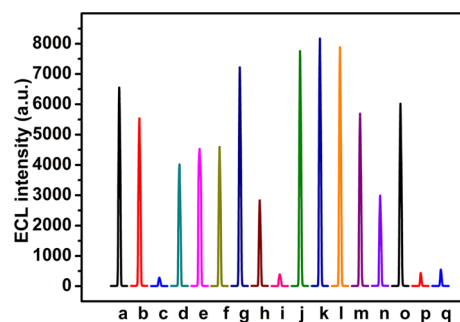

Figure 4. ECL assay of 17 different pig serum samples without any reference test to classify pigs as truly infected or noninfected (compared to ELISA at a dilution ratio of 1:100). The detailed ECL intensity values of 17 serum samples were presented in the Supporting Information.

For comparison, some other proposed methods for the determination of PrV antibody are presented in Table S2 (Supporting Information), showing that the current biosensor had a better performance than some methods reported previously, especially in terms of detection limit.[45]

Amplification Effect of the Triple or Multiple ECL Biosensor. The role of three amplifying medium (graphene, silica nanosphere, and biotin−strepavidin) were confirmed by contrasting the signal intensities of five different biosensors (Figure 5). As it can be seen from curve a, curve b and curve c, the first biosensor with a low ECL intensity can be used as the blank control experiment (curve a). Compared curve b to curve a, the enhanced ECL intensity indicated that gold nanoparticles had better adsorption capacity to attach antibodies. And
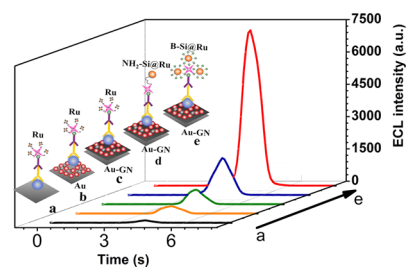

Figure 5. ECL responses of (a) Ru(BPY)$_3$/SA/B-Ab$_2$/Ab$_1$/BSA/Ag/ GCE, (b) Ru(BPY)$_3$/SA/B-Ab$_2$/Ab$_1$/BSA/Ag/Au NPs/GCE, (c) Ru(BPY)$_3$/SA/B-Ab$_2$/Ab$_1$/BSA/Ag/Au−GN/GCE, (d) NH$_2$−Ru@ SNPs/SA/B-Ab$_2$/Ab$_1$/BSA/Ag/Au−GN/GCE, and (e) B−Ru@ SNPs/SA/B-Ab$_2$/Ab$_1$/BSA/Ag/Au−GN/GCE.
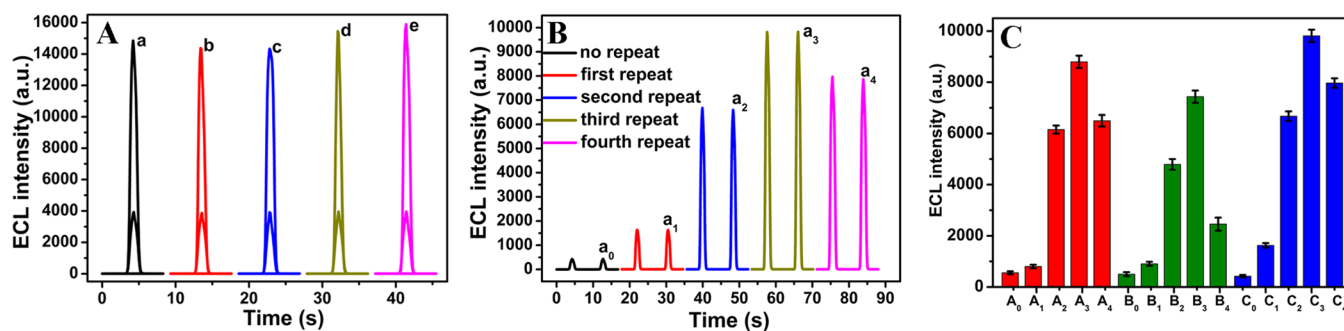
Figure 6. (A) Reproducibility of the first repetition of the "growth" step (five B−Ru@NPs/SA/B-Ab$_2$/Ab$_1$/BSA/Ag/Au−GN/GCE at an identical concentration of PrV antibody). (B) The effect of signal amplification with 4 continuous repetitions: (a_0) no, (a_1) first, (a_2) second, (a_3) third, and (a_4) fourth. (C) Effects of signal amplifications with 4 continuous repetitions at a dilution ratio of (A_0−A_4) 1:10^5, (B_0−B_4) 1:10^6, and (C_0−C_4) 1:10^7.

compared curve c to curve b, the ECL intensity was improved 1.9-fold which demonstrated that GN not only accelerated the electron transfer, but also provided a large surface area to attach more gold nanoparticles. Compared Ru(bpy)$_3^{2+}$ encapsulated silicon nanoparticles (Ru@SNPs) to Ru(BPY)$_3$ (curve d and curve c), the ECL intensity was enhanced 2.5-fold after introducing silica nanoparticles because of the connection of the enhanced signal labels in single immunization event. From curve e and curve d, the ECL intensity was enhanced 4.1-fold which could be attributed to two reasons: (i) the interaction of biotin−streptavidin is much greater than electrostatic adsorption and (ii) one streptavidin can contact extra three biotinylated Ru(bpy)$_3^{2+}$ encapsulated silica nanoparticles (B−Ru@SNPs).

For confirming the feasibility and reproducibility of the "growth" step, the first repetition of the "growth" step was carried out by a sequential modification of SA and B−Ru@SNPs onto five biosensors (B−Ru@SNPs/SA/B-Ab$_2$/Ab$_1$/BSA/Ag/Au−GN/GCE) with an identical concentration of Ab$_1$ (dilution ratio 1:10^7). As shown in Figure 6A, the five modified biosensors exhibited about a 4-fold magnification in the ECL intensity with a relative error of less than 6%, indicating the good feasibility and reproducibility of the "growth" step repetition.

The limit of signal amplification was investigated by continuous repetitions of the "growth" step on one biosensor (dilution ratio 1:10^7). As shown in Figure 6B, 3.8-fold, 15.7-fold, and 23.1-fold increases in the ECL intensity were obtained respectively from the three repetitions. The dominant reason for the continuous amplification improvement was related to the loading of an increasing number of signal labels. However, after the fourth repetition, a clear decrease occurred in the ECL intensity, because of the block of the electron transfer between the electrode interface and electrolyte induced by the nonconductive materials. To achieve the maximum amplification with the minimum steps, the fifth repetition was not carried out. Thus, the optimum amplification effect could be obtained via three repetitions.

Figure 6C shows the signal amplification performance of several repetitions on three different biosensors (B−Ru@SNPs/SA/B-Ab$_2$/Ab$_1$/BSA/Ag/Au−GN/GCE, dilution ratio 1:10^5, 1:10^6, and 1:10^7). With an increase of repetition times, the signal intensities of all the ECL biosensors gradually increased in the first three repetitions, but deceased after the fourth repetition. This phenomenon clearly demonstrated that the continuous-repetition method is feasible and reliable for achieving multiple and tunable signal amplification. Never-

theless, no definite regularity between the magnification and the concentration of Ab$_1$ was found in all the four repetitions owing to the delicate relations of the three crucial factors: steric hindrance, the number of signal labels and mass transfer resistance. In the first repetition, the magnification of A_1/A_0 by 1.5-fold, B_1/B_0 by 1.8-fold, and C_1/C_0 by 3.8-fold was obtained with a decrease of Ab$_1$, probably because the steric hindrance of B−Ru@SNPs became the crucial factor against the number of signal labels. Although the triple biosensor with a loading of more targets has captured more signal labels, the residual narrow gap between each of B−Ru@SNPs on the outermost layer hinders the further assembling of signal labels in the next step. Therefore, the triple biosensor with a loading of fewer targets has a better magnification effect. Only via the first repetition the outermost layer of any biosensor will be covered with adequate signal labels, and with the subsequent continuous repetitions, an increasing number of signal labels will be attached to the surface of each biosensor, resulting in a gradual amplification. With two further repetitions of the process, the theoretic dynamic balance could be achieved because of the interdependence and mutual restraint of the two key factors: the number of signal labels and the mass transfer resistance. Finally, the reductive signal intensity caused by that the mass transfer resistance will prevail over the number of signal labels.

■ CONCLUSIONS

In this study, a novel ECL detection strategy for PrV antibody has been developed based on Au−GN hybrids, silica nanoparticles and biotin−streptavidin (B−SA). Most importantly, the novel stretch−stowage−growth strategy was proposed for achieving the multiplex and adjustable amplification. Three conclusions could be drawn for the dramatic signal amplification: (i) the introduction of Au−GN nanosheet onto the immunosensor surface efficiently accelerated the electron transfer and enlarged the relative surface active region; (ii) a large amount of Ru(bpy)$_3^{2+}$ was encased in the silica nanoparticles to enhance the ECL detection signal; and (iii) biotin−streptavidin conjunction not only improved the amount of immobilized Ab$_2$ for the triple signal amplification but also achieved the tunable multiple amplification by repeating the formation of the B−SA−B structure. Compared with the traditional ELISA and emerging fluorescence analysis, the current low-cost method exhibited a higher sensitivity, wider linear range and better specificity, reproducibility, and stability. Furthermore, the three-step process could be used as a universal "mode" for detecting other biological samples with some minor changes. The novel detection strategy could be

used as an important tool for clinical diagnosis and evaluation of immunological efficiency, as well as early prevention of further disease progression.

■ ASSOCIATED CONTENT

ⓢ Supporting Information

FT-IR spectra, Raman spectra, photos, PL spectra, EIS, CV, reaction equation, SEM, optimizing incubation time and pH, and comparative data of determination results. This material is available free of charge via the Internet at http://pubs.acs.org/.

■ AUTHOR INFORMATION

Corresponding Author

*Tel: +86-27-87288505. Fax: +86-27-87288505. E-mail: hyhan@mail.hzau.edu.cn.

Notes

The authors declare no competing financial interest.

■ ACKNOWLEDGMENTS

■ REFERENCES

(1) Mettenleiter, T. C. *Vet. Res.* **2000**, *31*, 99−115.

(2) (a) Iglesias, G.; Pijoan, C.; Molitor, T. *Arch. Virol.* **1989**, *104*, 107−115. (b) Kimman, T. G.; Wind, N. d.; Oei-Lie, N.; Pol, J. M. A.; Berns, A. J. M.; Gieikens, A. L. J. *J. Gen. Virol.* **1992**, *73*, 243−251.

(3) Ben-Porat, T.; DeMarchi, J. M.; Lomniczi, B.; Kaplan, A. S. *Virology* **1986**, *154*, 325−334.

(4) Mellencamp, M.; Pfeiffer, N.; Suiter, B.; Harness, J.; Beckenhauer, W. *J. Clin. Microbiol.* **1989**, *27*, 2208−2213.

(5) Li, X.; Chen, K.; Huang, L.; Lu, D.; Liang, J.; Han, H. *Microchim. Acta* **2012**, *180*, 303−310.

(6) Ma, W.; Lager, K. M.; Richt, J. A.; Stoffregen, W. C.; Zhou, F.; Yoon, K. J. *J. Vet. Diagn. Invest.* **2008**, *20*, 440−447.

(7) Dodeigne, C.; Thunus, L.; Lejeune, R. *Talanta* **2000**, *51*, 415−439.

(8) (a) Liu, H.; Xu, S.; He, Z.; Deng, A.; Zhu, J. *Anal. Chem.* **2013**, *85*, 3385−3392. (b) Xu, S.; Liu, Y.; Wang, T.; Li, J. *Anal. Chem.* **2011**, *83*, 3817−3823. (c) Wang, J.; Han, H.; Jiang, X.; Huang, L.; Chen, L.; Li, N. *Anal. Chem.* **2012**, *84*, 4893−4899.

(9) (a) Chen, Y.; Xu, J.; Su, J.; Xiang, Y.; Yuan, R.; Chai, Y. *Anal. Chem.* **2012**, *84*, 7750−7755. (b) Kurita, R.; Arai, K.; Nakamoto, K.; Kato, D.; Niwa, O. *Anal. Chem.* **2012**, *84*, 1799−1803.

(10) Gámiz-Gracia, L.; García-Campaña, A. M.; Huertas-Pérez, J. F.; Lara, F. J. *Anal. Chim. Acta* **2009**, *640*, 7−28.

(11) Richter, M. M. *Chem. Rev.* **2004**, *104*, 3003−3036.

(12) Miller, C. J.; McCord, P.; Bard, A. J. *Langmuir* **1991**, *7*, 2781−2787.

(13) Sato, Y.; Uosaki, K. *J. Electroanal. Chem.* **1995**, *384*, 57−66.

(14) Choi, H. N.; Cho, S. H.; Lee, W. Y. *Anal. Chem.* **2003**, *75*, 4250−4256.

(15) (a) Wu, Y.; Zhou, H.; Wei, W.; Hua, X.; Wang, L.; Zhou, Z.; Liu, S. *Anal. Chem.* **2012**, *84*, 1894−1899. (b) Jiang, X.; Chen, K.; Han, H. *Biosens. Bioelectron.* **2011**, *28*, 464−468. (c) Li, L.; Liu, K.; Yang, G.; Wang, C.; Zhang, J.; Zhu, J. *Adv. Funct. Mater.* **2011**, *21*, 869−878.

(16) Li, J.; Guo, L. R.; Gao, W.; Xia, X. H.; Zheng, L. M. *Chem. Commun.* **2009**, *48*, 7545−7547.

(17) (a) Zhao, X.; Zhou, S.; Jiang, L.; Hou, W.; Shen, Q.; Zhu, J. *Chem.—Eur. J.* **2012**, *18*, 4974−4981. (b) Zhang, S.; Shao, Y.; Liao, H.-g.; Liu, J.; Aksay, I. A.; Yin, G.; Lin, Y. *Chem. Mater.* **2011**, *23*, 1079−1081. (c) Wang, S.; Wang, X.; Jiang, S. P. *Phys. Chem. Chem. Phys.* **2011**, *13*, 6883−6891.

(18) Yoon, S. B.; Sohn, K.; Kim, J. Y.; Shin, C. H.; Yu, J. S.; Hyeon, T. *Adv. Mater.* **2002**, *14*, 19−21.

(19) Zhu, Q.; Han, M.; Wang, H.; Liu, L.; Bao, J.; Dai, Z.; Shen, J. *Analyst* **2010**, *135*, 2579−2584.

(20) (a) Yin, X.; Qi, B.; Sun, X.; Yang, X.; Wang, E. *Anal. Chem.* **2005**, *77*, 3525−3530. (b) Gan, X.; Yuan, R.; Chai, Y.; Yuan, Y.; Mao, L.; Cao, Y.; Liao, Y. *Biosens. Bioelectron.* **2012**, *34*, 25−29.

(21) Gao, W.; Xia, X.; Xu, J.; Chen, H. *J. Phys. Chem. C* **2007**, *111*, 12213−12219.

(22) (a) Wang, L.; Yang, C.; Tan, W. *Nano Lett.* **2005**, *5*, 37−43. (b) Zhu, X.; Chen, L.; Lin, Z.; Qiu, B.; Chen, G. *Chem. Commun.* **2010**, *46*, 3149−3151. (c) Lin, Z.; Chen, L.; Zhu, X.; Qiu, B.; Chen, G. *Chem. Commun.* **2010**, *46*, 5563−5565. (d) Chen, L.; Cai, Q.; Luo, F.; Chen, X.; Zhu, X.; Qiu, B.; Lin, Z.; Chen, G. *Chem. Commun.* **2010**, *46*, 7751−7753.

(23) Zhang, L.; Liu, B.; Dong, S. *J. Phys. Chem. B* **2007**, *111*, 10448−10452.

(24) Rubinstein, I.; Bard, A. J. *J. Am. Chem. Soc.* **1980**, *102*, 6641−6642.

(25) Zhang, L.; Dong, S. *Anal. Chem.* **2006**, *78*, 5119−5123.

(26) Lin, D.; Wu, J.; Wang, M.; Yan, F.; Ju, H. *Anal. Chem.* **2012**, *84*, 3662−3668.

(27) Liao, N.; Zhuo, Y.; Chai, Y.; Xiang, Y.; Cao, Y.; Yuan, R.; Han, J. *Chem. Commun.* **2012**, *48*, 7610−7612.

(28) Egashira, N.; Morita, S. I.; Hifumi, E.; Mitoma, Y.; Uda, T. *Anal. Chem.* **2008**, *80*, 4020−4025.

(29) (a) Xiang, Y.; Zhang, H.; Jiang, B.; Chai, Y.; Yuan, R. *Anal. Chem.* **2011**, *83*, 4302−4306. (b) Chen, Y.; Jiang, B.; Xiang, Y.; Chai, Y.; Yuan, R. *Chem. Commun.* **2011**, *47*, 7758−7760.

(30) Chen, Z.; Liu, Y.; Wang, Y.; Zhao, X.; Li, J. *Anal. Chem.* **2013**, *85*, 4431−4438.

(31) Bae, S. W.; Cho, M. S.; Hur, S. S.; Chae, C. B.; Chung, D. S.; Yeo, W. S.; Hong, J. I. *Chem.—Eur. J.* **2010**, *16*, 11572−11575.

(32) Han, J.; Zhuo, Y.; Chai, Y.; Xiang, Y.; Yuan, R.; Yuan, Y.; Liao, N. *Biosens. Bioelectron.* **2013**, *41*, 116−122.

(33) Hou, L.; Gao, Z.; Xu, M.; Cao, X.; Wu, X.; Chen, G.; Tang, D. *Biosens. Bioelectron.* **2014**, *54*, 365−371.

(34) Lin, D.; Wu, J.; Ju, H.; Yan, F. *Biosens. Bioelectron.* **2014**, *52*, 153−158.

(35) Novoselov, K. S.; Geim, A. K.; Morozov, S. V.; Jiang, D.; Zhang, Y.; Dubonos, S. V.; Grigorieva, I. V.; Firsov, A. A. *Science* **2004**, *306*, 666−669.

(36) Bertoncello, P.; Forster, R. J. *Biosens. Bioelectron.* **2009**, *24*, 3191−3200.

(37) (a) Frens, G. *Nature* **1973**, *241*, 20−22. (b) Kovtyukhova, N. I.; Ollivier, P. J.; Martin, B. R.; Mallouk, T. E.; Chizhik, S. A.; Buzaneva, E. V.; Gorchinskiy, A. D. *Chem. Mater.* **1999**, *11*, 771−778. (c) Liu, K.; Zhang, J.; Yang, G.; Wang, C.; Zhu, J. *J. Electrochem. Commun.* **2010**, *12*, 402−405.

(38) Qian, J.; Zhou, Z.; Cao, X.; Liu, S. *Anal. Chim. Acta* **2010**, *665*, 32−38.

(39) Shan, C.; Yang, H.; Han, D.; Zhang, Q.; Ivaska, Ari; Niu, L. *Langmuir* **2009**, *25*, 12030−12033.

(40) Yang, D.; Rochette, J. F.; Sacher, E. *J. Phys. Chem. B* **2005**, *109*, 4481−4484.

(41) Liang, J.; Chen, Z.; Guo, L.; Li, L. *Chem. Commun.* **2011**, *47*, 5476−5478.

(42) Tai, Y.; Watanabe, M.; Murakami, J.; Tajiri, K. *J. Mater. Sci.* **2007**, *42*, 1285−1292.

(43) Plinio Innocenzi, H. K.; Toshinobu, Yoko. *J. Phys. Chem. B* **1997**, *101*, 2285−2291.

(44) Zu, Y.; Bard, A. J. *Anal. Chem.* **2001**, *73*, 3960−3964.

(45) (a) Li, F.; Zhou, R.; Zhao, K.; Chen, H.; Hu, Y. *Talanta* **2011**, *87*, 302−306. (b) Li, X.; Chen, K.; Huang, L.; Lu, D.; Liang, J.; Han, H. *Microchim. Acta* **2012**, *180*, 303−310.